

Geometric Effects in Large Scale Intracellular Flows

Olenka Jain^{1,2}, Brato Chakrabarti³, Reza Farhadifar², Elizabeth R. Gavis⁴, Michael J. Shelley^{2,5}, and Stanislav Y. Shvartsman^{2,4,1}

¹Lewis-Sigler Institute for Integrative Genomics, Princeton University, Princeton, New Jersey 08544, USA

²Center for Computational Biology, Flatiron Institute, New York, New York 10010, USA

³International Center for Theoretical Sciences, Bengaluru 560089, India

⁴Department of Molecular Biology, Princeton University, Princeton, New Jersey 08544, USA

⁵Courant Institute, New York University, New York, New York 10012, USA



(Received 3 September 2024; accepted 1 April 2025; published 8 May 2025)

This work probes the role of cell geometry in orienting self-organized fluid flows in the late-stage *Drosophila* oocyte. Recent theoretical work has shown that a model, which relies only on hydrodynamic interactions of flexible, cortically anchored microtubules and the mechanical loads from molecular motors moving upon them, is sufficient to generate observed flows. While the emergence of flows has been studied in spheres, oocytes change shape during streaming, and it was unclear how robust these flows are to the geometry of the cell. Here we use biophysical theory and computational analysis to investigate the role of geometry and find that the axis of rotation is set by the shape of the domain and that the flow is robust to biologically relevant perturbations of the domain shape. Using live imaging and three-dimensional flow reconstruction, we test the predictions of the theory/simulation, finding consistency between the model and live experiments, further demonstrating a geometric dependence on flow direction in late-stage *Drosophila* oocytes.

DOI: 10.1103/PRXLIFE.3.023007

I. INTRODUCTION

Symmetry breaking is a fundamental process in biology, critical for development and organization, from subcellular structures to whole body organization. Biological systems employ myriad internal and external cues, such as chemical gradients and force imbalances to break symmetries. Here we examine the role of a less well characterized source of asymmetry: the shape of the domain in which dynamics play out [1,2]. Our work is motivated by self-organized cell-scale fluid flows, referred to as cytoplasmic streaming, associated with a cortically bound bed of flexible microtubule fibers under motor protein loads in the *Drosophila* oocyte. The flows are critical for transporting material in the late-stage *Drosophila* oocyte, where the large size of the cell limits the efficiency of diffusion-based transport [3–5]. Without flows, specific mRNA molecules that are critical for setting up the chemical gradients that prepattern the *Drosophila* embryo are improperly localized and result in disrupted development. Understanding how such self-organizing systems pick a direction for flow is critical for quantifying their transport and mixing properties. Here, we examine whether the geometry of the cell can determine the direction and structure of these flows.

This paper is organized as follows. First, we perform large-scale hydrodynamic simulations in ellipsoidal geometries of a fluid structure model based on recent theoretical work on cytoplasmic streaming [6]. We find relaxation to vortical

steady states, consistent with earlier theoretical work that found vortical steady states in spherical geometries [4]. Furthermore, we find a secondary relaxation from the initial vortical state aligned with any random direction, to a stable state in which the vortex rotates around the long axis of the ellipsoid. We call such flows “axisymmetric.” Second, we test the prediction of axisymmetrization experimentally in stage-12 *Drosophila* oocytes, which are approximately ellipsoidal. This allows us to conjecture that the flow patterns are robust and that they tend to be aligned with the long axis of the cell. Additionally, we find that the handedness of the flow is unbiased, as would be expected from a symmetry-breaking system. Finally, we probe the robustness of such vortical flows with a coarse-grained continuum model that allows us to easily explore steady-state solutions to other geometric perturbations, such as intracellular obstacles in the form of a cell nucleus.

The simplest setting for our problem is a closed domain containing a Stokes fluid and uniformly covered with motor-loaded slender filaments attached to the surface [6,7] [Fig. 1(a)]. This model is based on the known biology of cytoplasmic streaming in the *Drosophila* oocyte. In the late-stage oocyte, stable microtubules (MTs) are cortically anchored to the cell cortex at their minus ends [8,9]. These MTs serve as railroads for the plus-end directed nanoscale molecular motors, kinesins, that carry cellular cargos [10,11]. By walking towards the free end of cortically anchored MTs, kinesin-cargo complexes exert a force on the cytoplasm, entraining the nearby fluid, and a compressive force on the inextensible MTs. For large compressive loads, the MTs can bend or buckle, leading to synergistic interactions between the deformations of the MTs and the flows they generate [12].

Published by the American Physical Society under the terms of the Creative Commons Attribution 4.0 International license. Further distribution of this work must maintain attribution to the author(s) and the published article's title, journal citation, and DOI.

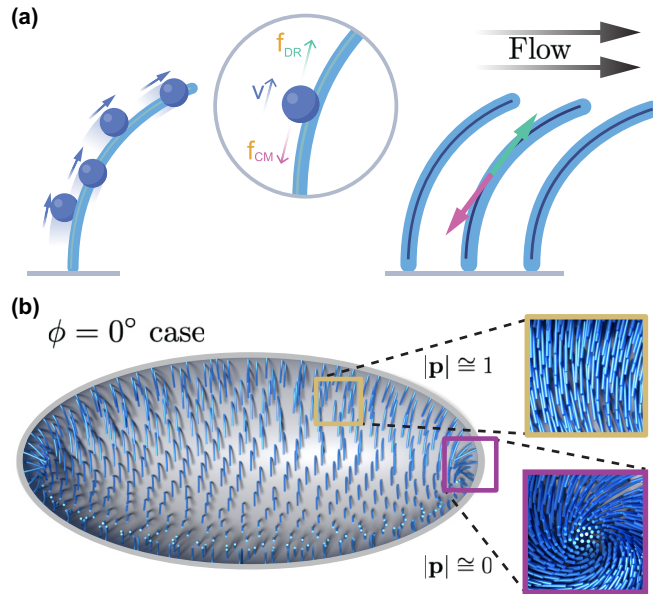


FIG. 1. Biophysical model for motor driven fluid flows: (a) Kinesin-cargo complexes (blue spheres) walk towards the free plus ends of anchored cortical MTs exerting both a drag force, f_{DR} , on the surrounding cytoplasm and a downwards compressive force, f_{CM} , on the inextensible MTs, causing them to bend. The model coarse-grains the kinesin-cargo forces as a uniform line density of forces, σ . (b) The orientation of microtubules in an ellipsoid during simulated flows. The flow rotates in line with the aligned MTs (yellow boxed detail) around the line connecting the defects (purple boxed detail). In ellipsoidal geometries, the defects go to the poles of the cell, which corresponds to flow around the long axis of the ellipsoid. The flow is characterized by ϕ , which measures the angle between the long axis of the ellipsoid and the axis of rotation of the flow.

A previous analysis of this model established that when the areal density of the MTs and the force from the motors was sufficiently high, the collective interactions resulted in the emergence of a self-sustained intracellular cell-scale vortical flow in a spherical geometry [4]. The vortical flow takes the form of rigid-body rotation plus a weak bitoroidal flow component [4]. However, oocytes are not spheres (the late-stage oocytes are well approximated by prolate ellipsoids), and cell geometry has nontrivial consequences for the emergent flows because it is nonlinearly coupled to the cytoplasmic flows [2,13,14]. Geometry breaks the rotational symmetry in the problem and poses the question of how the interior flow is topologically organized. What sets the axis and chirality of the emergent flows? The present study examines these questions, which are central to understanding the potential functions of streaming flows.

II. RESULTS

A. Large scale hydrodynamic simulations in ellipsoidal geometries

Following previous work, the joint dynamics of microtubules (MTs) coupled through a viscous fluid are described [7]. The microtubule density is assumed to be uniform in

the absence of any evidence of inhomogeneity in late-state oocytes, and the microtubule length is set at 20 μm , given the results of previous imaging work [4]. The evolution of each microtubule $\mathbf{X}^i(s, t)$, parametrized by arc length s , time t , and in a background velocity field \mathbf{u} , evolves as

$$\eta(\mathbf{X}_t^i - \bar{\mathbf{u}}_i) = (\mathbf{I} + \mathbf{X}_s^i \mathbf{X}_s^i) \cdot (\mathbf{f}^i - \sigma \mathbf{X}_s^i), \quad (1)$$

$$\mathbf{f}^i = -E \mathbf{X}_{sss}^i + (T^i \mathbf{X}_s^i)_s, \quad (2)$$

where $\bar{\mathbf{u}}_i$ accounts for the fact that we only consider the non-local contributions to the velocity field by the fibers. In other words, $\bar{\mathbf{u}}_i$ is the velocity field induced by every other fiber that is not the i th fiber. The forces governing the dynamics of the fiber are \mathbf{f}^i , the elastic force per unit length from microtubule bending, and σ , the coarse-grained compressive force due to the movement of motor-cargo complexes. I is the identity matrix, E is the bending rigidity, T^i is the MT tension, which acts as a Lagrange multiplier to enforce the incompressibility of each fiber, and η is the drag coefficient. The drag coefficient on the slender fiber is given by $\eta = \frac{8\pi\mu}{|c|}$, where μ is the viscosity and $c = \log ee^2$ is a coefficient characterizing the slenderness of the MT (e is the ratio of MT length to width). Each MT fiber is clamped normally to the cortex, and the free end is both force- and torque-free.

The left half of Fig. 1(a) shows the forces on a single MT from drag and compression, and the resultant bending of the MT. The right half of Fig. 1(a) illustrates the coarse graining of force from the motor-cargo complexes to a uniform line density of forces as well as the resultant flow field generated in the surrounding cytoplasm. The flow of the cytoplasm is governed by the forced incompressible Stokes equation, and it is subject to a no-slip boundary condition at the cortex:

$$\nabla q - \mu \Delta \mathbf{u} = \sum_{i=1}^N \int_0^L ds \mathbf{f}^i(s) \delta(\mathbf{x} - \mathbf{X}^i), \quad (3)$$

$$\nabla \cdot \mathbf{u} = 0, \quad (4)$$

where q is pressure and \mathbf{u} is the velocity field.

We used large scale hydrodynamic simulations (SkellySim) to evolve fibers according to Eqs. (1) and (2) in a background fluid subject to Eqs. (3) and (4) in ellipsoidal geometries [15]. The result of a representative simulation is visualized in Fig. 1(b). As in the case of the sphere, vortical flow emerged as the long-term state of the problem. However, in the case of the ellipsoid, the axis of rigid-body rotation was independent of initial conditions and consistently close to the long axis of the ellipsoid. The code was previously tested and validated to ensure that there was no intrinsic handedness that might determine the emergent vortical flows [4]. The handedness of the flow was therefore the result of spontaneous symmetry breaking, and we observed no bias in clockwise or counterclockwise flows. We characterized the flow rotation by ϕ , the angle of inclination made by the vortical axis to the long axis of the cell. Completely aligned axisymmetric flow is characterized by $\phi = 0^\circ$.

To determine the axis of flow rotation, we made use of the fact that the flow field rotates around the line connecting “defects” in the MT fiber bed. We define “defects” as locations on the surface where fibers are locally unaligned. Vortical

flow is characterized by a largely bent or “combed over” bed of fibers with two defects at opposite ends of the cell. Just as combing a hairy ball results in at least two topological defects, the fibers are not able to all bend over in such a way that their directions are always locally aligned, and instead two “defects” form. An example of a defect is shown by the rightmost purple boxed detail in Fig. 1(b).

To calculate the defect location, we use the surface polarity field as previously done in Ref. [4]. The vector $\mathbf{p}^i(t)$ is defined as the projection of fiber i onto the local tangent plane:

$$\mathbf{p}^i(t) = (\mathbf{I} - \mathbf{n}\mathbf{n}) \cdot \frac{\mathbf{X}^i(L, t) - \mathbf{X}^i(0, t)}{L}, \quad (5)$$

where L is the length of the MT, and \mathbf{n} is the inward surface normal at $\mathbf{X}^i(0, t)$. The surface polarity field $\mathbf{p}(t)$ is a local average of $\mathbf{p}^i(t)$ vectors. When the fibers are highly bent and aligned in the same direction, $|\mathbf{p}(t)|$ is close to and bounded by 1. A representative example of locally aligned fibers is shown by the yellow boxed detail in Fig. 1(b). When the fibers are unaligned, $|\mathbf{p}(t)|$ is close to 0. Further details are provided in the Supplemental Material [2,3,16].

Simulations from an initially straight bed of fibers relaxed to a vortical flow with two $|\mathbf{p}| \cong 0$ defects in MT order. In ellipsoidal geometries, the initial locations of the two defects were strongly dependent upon initial conditions and possibly far from alignment with the long axis. The two defects then slowly moved from their initial position of formation towards the poles of the ellipsoid, resulting in a nearly axisymmetric flow state at long times. This movement of defects from their initial position to their resting place at the poles was associated with a decrease in total elastic energy, the governing energy in this low Reynolds number, bending driven flow. The elastic energy \mathcal{E} is directly proportional to the squared curvature of the fibers and is defined as

$$\mathcal{E}(t) = \frac{E}{2} \sum_{i=1}^N \int_0^{L^i} ds [\kappa^i(s, t)]^2, \quad (6)$$

where N is the number of fibers and κ is the curvature along the fiber. The elastic energy comes from the movement of molecular motors on the fibers, causing them to bend. The energy is dissipated in the form of viscous drag in the fluid flows.

B. Analysis of velocity fields from simulations in ellipsoidal geometries

To investigate the stability of the “axisymmetric” flow state in an ellipsoid, we performed numerical “perturbation” experiments in which we evolved flow in a sphere until steady state. We then stretched the sphere perpendicular to the axis of rotation of flow while maintaining the same surface area and MT placement. We ensured that the boundary condition of normally clamped fibers was met. We allowed the system to evolve from this vortical state where the initial axis of rotation was $\phi = 90^\circ$. The final ϕ was calculated and converged to 0° as the ellipsoid became increasingly elongated [Fig. 2(a)]. This was true for ellipsoids with aspect ratios ranging from 1.2 to 2.2 (the aspect ratios we found in late-stage *Drosophila* oocytes). The elastic energy of the steady state was lowest in ellipsoids with the highest aspect ratios.

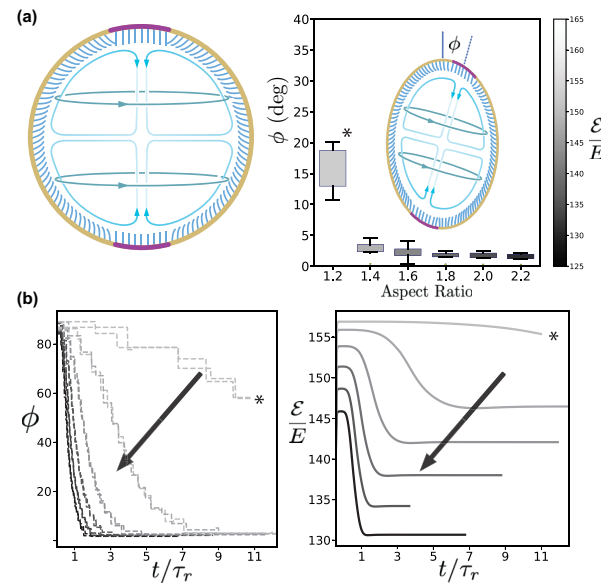


FIG. 2. The effect of cell geometry on final flow orientation from numerical experiments: (a) The structure of flow in a spherical geometry flow is largely solid body rotation with a small bitoiodal component due to the closed geometry. Defects appear at opposite ends of the sphere (highlighted in purple). Five simulations in each ellipsoid of the aspect ratio (AR) ranging from 1.2 to 2.2 robustly show that the steady-state location of the defects/axis of rotation (defined by ϕ) is consistently nearly or exactly at the poles of the ellipsoid. The * represents the fact that the 1.2 AR ellipsoid simulation did not converge, and so while its trajectory is consistent with a final axisymmetric state, the simulations only show part of the trajectory. The elastic energy of the final state is minimized as the aspect ratio of the ellipsoid is increased. (b) The location of each of the two +1 defects as a function of simulation time is shown for ellipsoids initialized with a steady-state flow field where $\phi = 90^\circ$ (left panel). ϕ converges to the axisymmetric flow case ($\phi = 0^\circ$) for ellipsoids with aspect ratios > 1 . The convergence to the axisymmetric flow state is associated with a minimization of elastic energy (right panel). The arrow represents increasing aspect ratios ranging from 1.2 (lightest gray) to 2.2 (black).

The effective dynamics can be rationalized as follows: because the surface area remains the same, the radius of the body of the ellipsoid decreases and the MTs become closer to each other. MTs across from each other are pushing and being pushed by the flow in opposite directions; they inhibit each other more and more as the long axis of the ellipsoid narrows. This leads to a relaxation of the MTs and a consequent decrease of elastic energy. The defects are the locations where the elastic energy is least in the bed, because it is there that the fibers are least bent.

We note that while we characterize the axis of rotation by defect placement, the defects are merely indicators of the flow’s global orientation. In other elastic systems, defects are important in organizing and driving the structure of the system. This is not the case here, where the structure is created by the bulk. To confirm this, we performed an additional simulation in which fibers were removed from the poles of a 1.4 AR ellipsoid. As with the unshorn simulations, an initial vortical state formed, having two defects and a rotational axis

spanning the short axis of the cell. Also as before, the vortical flow reoriented to rotate around the long axis. In the final state, there were no defects in the fiber bed because there were no fibers at the poles, yet we still observed the global reorientation of the flow to rotate along the long axis. Details of this simulation can be found in the Supplemental Material [16].

The total elastic energy of the microtubule bed is the natural energy of the system [17]. In the Supplemental Material [16], we show that for this active system, the elastic energy is reduced by viscous shear dissipation and frictional drag on the fiber, whereas the input power comes from the work done by active kinesin motors. The vortical states that we observe are a balance between these effects. By a scaling argument for thin active layers, we find that vortical states are a balance between the input power and the frictional drag alone. The viscous dissipation is subdominant, with its largest component being the viscous dissipation in the bed, rather than in the bulk, due to the steep velocity gradients there; for details, see the Supplemental Material [16].

The timescale of evolution to the “axisymmetric” state occurs on the order or $\tau_r = \frac{\eta L^4}{E}$, the single MT relaxation timescale, which is the longest timescale of the system. The two other relevant timescales in this system are τ_c , the collective MT relation timescale, and τ_m , the timescale associated with a motor moving an MT its own length [4]. Additionally, we found that this relaxation, which can be well fit by an exponential decay, was proportional to the aspect ratio. The higher the aspect ratio, the shorter the lifetime of the decay, λ . In other words, elongated ellipsoids were able to more quickly reach steady state [Fig. 2(b)].

Finally, in order to interpret experimental data, which can be obtained from thin cortical slices of the cell, we characterized velocity streamlines on cortical slices from simulation data to predict what would be seen by a confocal microscope for different ϕ values. Defining the long axis of the cell as X and the height as Z , we found that the relative magnitudes of the three-component velocity field differed between $\phi = 0^\circ$ and 90° flow (Fig. 3). When the velocity field is axisymmetric ($\phi = 0^\circ$), v_x is minimized. On the other hand, when the axis of rotation is perpendicular to the long axis of the cell ($\phi = 90^\circ$), the component of flow along the long axis, v_x , dominates.

C. Live imaging and particle tracking

Next, we turned to experiments to test the predictions of the numerical analysis: (i) that cell geometry plays a role in setting the direction of the flow field in *Drosophila* oocytes, and (ii) the sense of rotation of the flow should be unbiased. While experiments observing flows in *Drosophila* oocytes date back to the 1980s, there has been no characterization of their handedness or axis of rotation [3,18].

Our experiments differ from previous experiments characterizing cytoplasmic streaming in *Drosophila* oocytes in three ways. First, we focused on late-stage oocytes where the cell is approximately ellipsoidal. In late-stage oocytes, the “dumping” process that delivers cytoplasm to the oocyte from the attached sister nurse cells is complete [3]. Flows in *Drosophila* oocytes can be broadly characterized as occurring before dumping, during dumping, and after dumping. Before dumping (stage 10), the oocyte geometry is complex and ill-

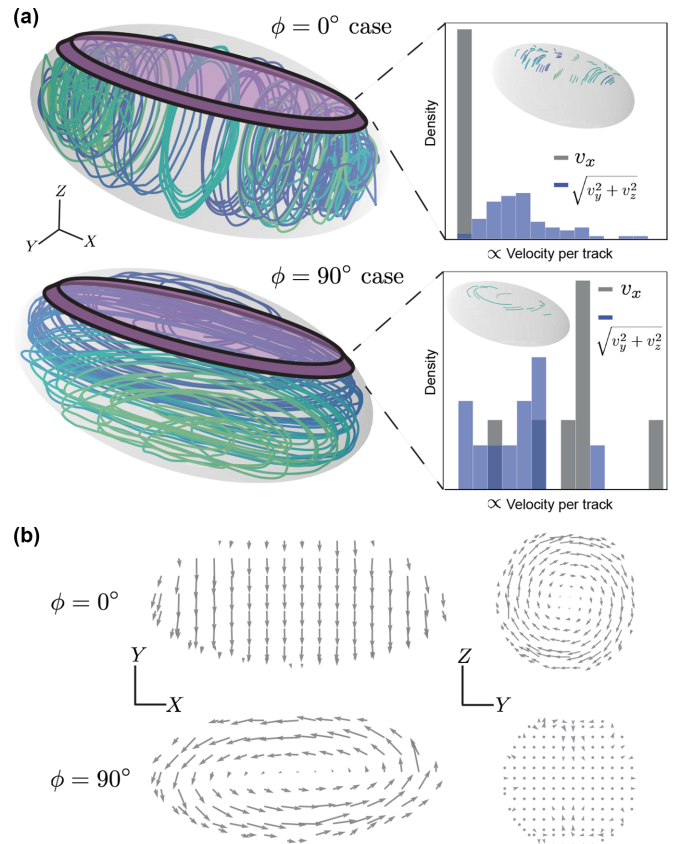


FIG. 3. The effect of flow orientation on cortical velocity fields from simulation: (a) Simulated streamlines from “axisymmetric flow” ($\phi = 0^\circ$), with flow around the long axis of the ellipsoid, and “vortex flow” ($\phi = 90^\circ$), with flow around the long axis of the ellipsoid. The relative magnitudes of v_x , v_y , and v_z in a thin cortical section as visualized by the purple volume discriminate between the “axisymmetric” and “vortex” flow cases. The ability to discriminate between flow orientations has implications for live-imaging, which can only access streaklines near the cortex of the oocyte. The x -axis is defined by the long axis of the ellipsoid. (b) The velocity field of the thin cortical slice for both $\phi = 0^\circ$ and 90° . In the x - y plane, v_y is dominant for axisymmetric flow, while v_x is dominant in fields where $\phi = 90^\circ$.

approximated by any simple geometry such as an ellipsoid. Additionally, a gradient of microtubules has been measured along the anterior-posterior axis [19–21]. During dumping (stage 11), the oocyte changes volume at a rate comparable to the velocity of the flow field, and there is an additional and significant input of volume from the nurse cells. This contribution of nurse cell flows renders the dynamics more complex than we currently model [22]. However, after dumping (stage 12), the flow from the nurse cells stops and the volume of the oocyte ceases to change rapidly with respect to the velocity of the flows. At stage 12, the oocyte geometry is well approximated by an ellipsoid. Lastly, confocal images of microtubules do not show any visible spatial gradient. By focusing on flow during this stage, we therefore avoided the confounding effects from dumping flows, complicated geometries, inhomogeneities in the microtubule bed, and any early flows that may not have reached steady state. Instead,

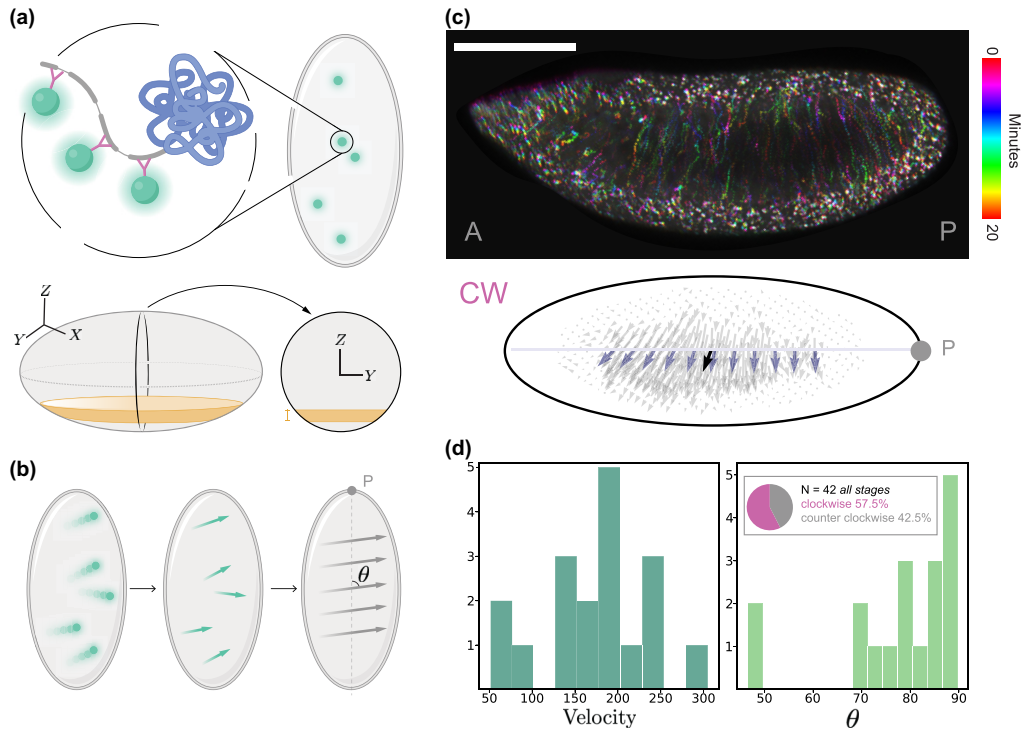


FIG. 4. Live imaging of inert particles and velocity field extraction: (a) Staufen proteins bound by multiple fluorescently protein tags aggregate and form inert tracer particles in stage-12 oocytes. These particles range from 0.5 to 2 μm in width. Using confocal imaging, we obtained 3D cortical slices as illustrated by the region highlighted in yellow. (b) The mean direction of flow, θ , was extracted from a maximum projection of the 3D cortical sections with a depth of 10–15 μm . The observed flow did not change direction in an experiment or simulation over 10–15 μm , which justified using the maximum projection. We tracked particles in each frame and linked the time points to extract trajectories. The trajectories were interpolated onto a structured grid to obtain a velocity field from which the overall mean angle of flow with respect to the long axis of the cell was computed. The handedness of the flow was determined with respect to the posterior end of the cell (gray dot). (c) An example of the experiment/analysis pipeline used to extract the velocity flow field with a mean direction, represented by the black arrow. The posterior of the cell is highlighted by the gray dot and “P”; scale bar = 100 μm . (d) In stage-12 oocytes, the distribution of maximum measured velocity in $\frac{\text{nm}}{\text{s}}$ is higher than that of stage-10 oocytes [4]. Across all stages of streaming (10–12), 57.5% rotated CW and 42.5% rotated CCW. The distribution of mean flow angles peaked around $\theta = 90^\circ$. This distribution is consistent with 3D flow fields where the defects are close to or at the poles ($\phi = 0^\circ$).

stage-12 flow provides an excellent approximation to test our numerical predictions.

Second, we performed the first experiments in which single-particle trajectories are visualized in the flow. To do so, we took advantage of a *Drosophila* strain expressing Staufen-SunTag [10] [Fig. 4(a)]. Staufen, an RNA-binding protein, is bound by multiple GFP-tagged nanobodies (SunTag), which results in a tendency to aggregate and create colloidal clumps of Staufen-SunTag molecules in the oocyte, with radii ranging from 500 nm to 2 μm . This generates fluorescently labeled particles throughout the oocyte cytoplasm that are advected by the flow and can be used as molecular tracers.

And lastly, we developed analytical methods to extract both individual particle tracks and velocity profiles, as well as characterize the flow orientation and handedness. We performed live confocal imaging of stage-12 oocytes expressing Staufen-SunTag [11]. Because the flow fields do not change dramatically slice to slice, the 10–15 μm stack of images was projected to maximize the available data. The particle tracking produced individual trajectories for each tracked particle [Fig. 4(b)].

Based on the observation that the trajectories tend to be aligned and perpendicular to the long axis, we used the

individual tracks to extract a velocity field from which we could get an average direction of flow. To do so, we made use of our knowledge about the flow field to interpolate the trajectories onto a structured grid. Because we observed that the fluid did not change directions locally, and because the fluid is incompressible, we assumed that the flow of a particle between two parallel trajectories is parallel and in the same direction. We thereby averaged information from the nearest neighbors of the known particle trajectories to points on a structured grid to generate an interpolated velocity field [Figs. 4(b) and 4(c)]. We observed that the velocity fields were largely vortex-free and that the average angle of flow was perpendicular to the long axis of the cell, which we defined by fitting an ellipsoid to the cell boundary.

To analyze the flow field, we characterized the velocity field by a single parameter: average angle of flow with respect to the long axis of the cell, θ [Fig. 4(b)]. We chose this method because the particle tracks were largely perpendicular to the long axis of the cell for nearly every oocyte imaged. We excluded examples with an obvious vortex by calculating the maximum curl of each velocity field and excluding examples that have points with a curl value above a threshold (there was only one such case).

Our simulations predicted that the axis of flow rotation should be aligned with the long axis of the oocyte. Our experimental results showed that the average angle of flow was peaked at 90° , which is consistent with flow rotating about the long axis of the cell. With the exception of one stage-12 oocyte (of 18 in total) in which flow appeared as a vortex, the measured flow fields were consistent with axisymmetric flow, as seen by the histogram in Fig. 4(d). Additionally, we measured the maximum velocity along the axisymmetric direction and found that on average, the maximum velocity of solid-body rotation was 180 nm/s. This is substantially higher than the velocities measured by in stage-10B oocytes, which had a maximum speed of 100 nm/s [4].

Likewise, our symmetry-breaking model and simulations predicted no bias in the handedness of the flows. From experiments, it was equally likely for a flow to be clockwise as it was counterclockwise [Fig. 4(d)].

We used the full three-dimensional (3D) particle tracks from the thin cortical slices to compare the imaged flow field with the simulated ones. Analysis of the streamlines of simulated flow fields revealed a pronounced difference in the relative magnitudes of the velocity components, v_x , v_y , and v_z , where the x -axis was defined by the long axis of the ellipsoid. If the flow field was close to axisymmetric, streamlines on cortical slices had $v_x < v_y, v_z$. If the flow field rotated perpendicular to the long axis of the cell, then the streamlines had $v_x > v_y, v_z$ (Fig. 3). Figure 5 shows that the analysis of experimental streamline velocity in two cases, axisymmetric and perpendicular to axisymmetric, is consistent with the predictions of simulated flow fields. In other words, measured flows with an average $\theta \cong 90^\circ$ are consistent with simulations of “axisymmetric” flows where $\phi = 0^\circ$.

D. 3D live light sheet imaging

Our experimental results using both cortical slices and thin 3D sections are consistent with an axisymmetric vortical flow. However, a full 3D flow field had yet to be measured in the *Drosophila* oocyte due to the difficulty of imaging such a large and dense sample. To overcome this, we developed a new technique to live-image oocytes in a multiview light sheet microscope, resulting in the first fully isotropic 3D visualization of cytoplasmic streaming [23]. Through this experiment, we have been able to find additional evidence to support our hypothesis.

Visual inspection of the flows revealed a clear vortical flow. As a first step in the quantitative analysis, we manually tracked the Staufen-SunTag particles and extracted streaklines [Figs. 6(b) and 6(c)]. The shadows from the yolk mean that it is not possible to visualize the motion of particles deep in the oocyte. Fortunately, it is the near-cortical flows that we are most interested in capturing to understand the direction and structure of the flow field.

To characterize the axis of flow rotation, ϕ , we compared the magnitude of velocity field along the long axis to that along the short axes. From our modeling, we expect that the ratio, $\frac{|v_x|}{\sqrt{v_y^2 + v_z^2}}$, is a monotonic function of ϕ , where the x -axis is the long axis of the ellipsoid. We fitted the boundary of the oocyte to a best-fit ellipsoid and calculated the values of polar and azimuthal angle flow. We compared these values to those

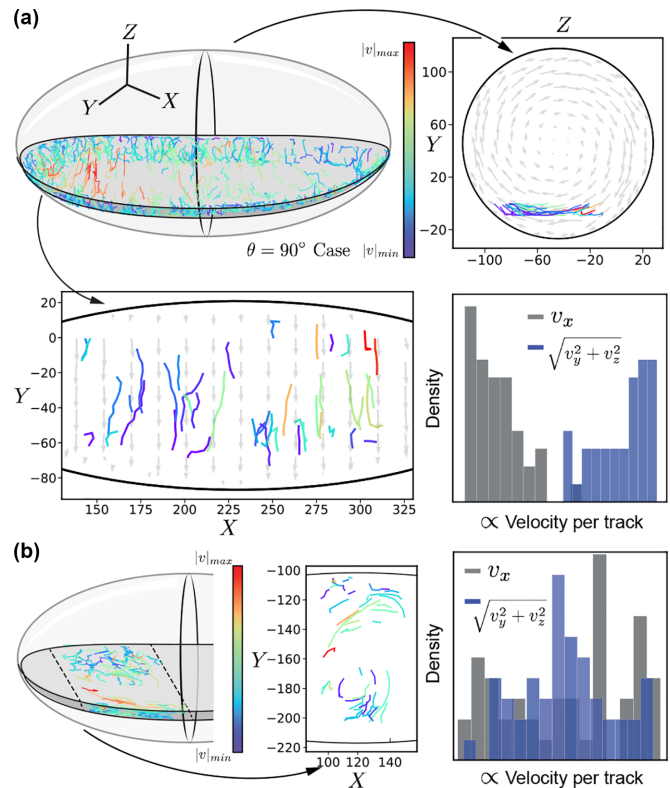


FIG. 5. Differentiating flow orientation from 3D single-particle tracks: (a) 3D particle tracks from a live imaging experiment with measured $\theta \cong 90^\circ$. The streamlines from both the short-axis and the long-axis perspective are overlaid on an axisymmetric velocity field as computed by simulation ($\phi = 0^\circ$). The x -axis is set by the long axis of the oocyte. The relative magnitudes of the streamlines from a cortical 3D volume with an average angle of flow $\theta \cong 90^\circ$ are consistent with those from simulated axisymmetric flow ($\phi = 0^\circ$) as seen in Fig. 1. (b) 3D particle tracks from the single experiment with a visible vortex. The distribution of velocity components per streamline is markedly different from the axisymmetric case.

at the equivalent coordinates from a dataset of 6552 simulated velocity fields. The simulated velocity fields in an ellipsoid with matching aspect ratio contained 91 values of ϕ , each with 72 rotations around the long axis. We used two methods to infer the angle of rotation of the flow. First, we calculated the mean-squared error between each simulation field and the data. Second, we calculated $\frac{|v_x|}{\sqrt{v_y^2 + v_z^2}}$ for each simulated field and found which flow best matched the ratio calculated from the data. There was significant agreement between the two methods, both predicting a defect at around $\phi = 21^\circ$.

While simulations predict a perfectly axisymmetric flow with $\phi = 0^\circ$, there could be many reasons for the mismatch. One such reason is that the simulations assume uniform placement of fibers and motor loading. Another is that the simulations assume a perfect ellipsoid for the shape of the oocyte. The actual cell is not an ellipsoid and instead somewhat arced like a banana. In summary, we observe a three-dimensional, nearly axisymmetric rotational flow field whose nature is consistent with the predictions of our 3D computational modeling, and which supports our statistical analyses of flows measured in near-cortical sections.

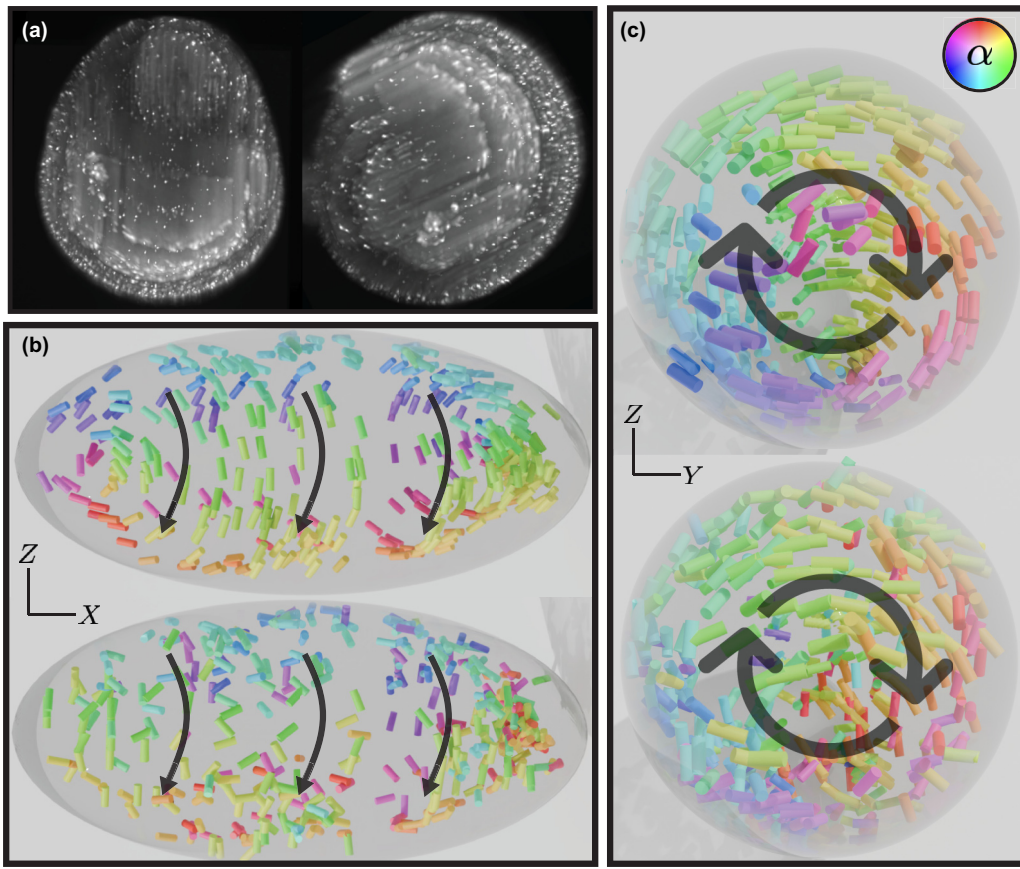


FIG. 6. Light sheet imaging of axisymmetric flow: (a) Staufen-SunTag particles are visible as white puncta from two views of the reconstructed light sheet image. The particles are brightest around the cortex. (b) Velocity vectors calculated from the manually tracked streaklines are shown for a simulation with $\phi = 21$ (top) and for the experiment (below). The shell represents the best-fitting ellipsoid to the boundary of the oocyte. The vectors are colored by the angle, α , of the velocity vector in the YZ plane. Black arrows show the direction of movement. Clear rotational flow is visible, where the axis of rotation is nearly the long axis of the cell (the x -axis).

E. Robustness to perturbation using the coarse-grained continuum model

To summarize our results so far, we found that flows can withstand geometric perturbations in the shape of the domain and that the axis of rotation is biased to be around the long axis. Another type of perturbation arises from internal structures, such as organelles. Though the geometry of the oocyte can be well approximated by an ellipsoid, the interior of the oocyte is densely packed with yolk granules, Golgi, endoplasmic reticulum, and various other cellular components. The largest of these components is the nucleus, with a radius of approximately $10 \mu\text{m}$, located near the anterior of the oocyte [Fig. 7(a)] [3,22,24]. It is thus natural to ask the following: How robust are the collective dynamics to large interior geometric perturbations that could alter the topology of the emergent flows?

This question can be most readily addressed using a recently proposed coarse-grained “active carpet” model in which we model the nucleus as a fixed no-slip surface [25]. In contrast to evolving the dynamics of individual MT filaments, the active carpet theory evolves a surface polarity field that quantifies the mean orientation of the MTs at a point. The model takes the form of a boundary force field coupled to an internal Stokesian flow, and it can be easily adapted to a range of self-organized, cortex-driven intracellular flows [25].

In this coarse-grained model, we characterize the dense MT carpet by a uniform areal density $\bar{\rho}$ and its orientation by a surface polarity field $\mathbf{P}(\mathbf{y}, t)$, where \mathbf{y} is the surface coordinate on the cell boundary. The polarity field evolves according to Jeffery’s equation as

$$\partial_t \mathbf{P} = (\mathbf{I} - \mathbf{P}\mathbf{P}) \cdot \nabla \mathbf{u}|_{\partial D} \cdot \mathbf{P} + \mathbf{T}_0 \times \mathbf{P}. \quad (7)$$

Here $\mathbf{u}(\mathbf{x}, t)$ is the internal cytoplasmic fluid velocity, ∂D is the cell boundary, and \mathbf{T}_0 is a restoring torque that mimics the bending response of a clamped filament by trying to align the microtubules with the local inward normal to the surface. The cytoplasmic fluid velocity is determined by solving the incompressible Stokes equation subject to the no-slip boundary condition on the cell surface. The activity of motor proteins driving the internal flow is coarse-grained as the surface stress jump $\mathbf{f}(\mathbf{y}, t)$ across an interface $\partial S := \partial D + \mathbf{n}(\mathbf{y})$ formed by the tips of the MT vectors. In dimensionless form, the momentum balance for the fluid flow reads

$$-\nabla q + \Delta \mathbf{u} = \mathbf{0}, \quad \nabla \cdot \mathbf{u} = 0, \quad (8)$$

$$\mathbf{u}(\mathbf{y}, t) = \mathbf{0} \quad \text{on } \partial D, \quad (9)$$

$$[\mathbf{u}] = \mathbf{0}, \quad [\sigma \cdot \mathbf{n}](\mathbf{y}, t) = -\bar{\mathbf{f}}(\mathbf{y}, t) \quad \text{on } \partial S. \quad (10)$$

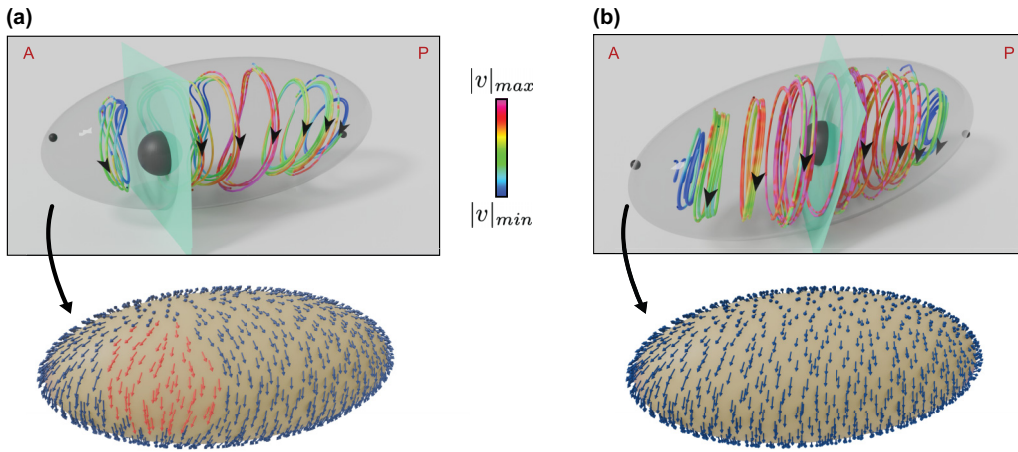


FIG. 7. The role of geometric obstacles in emergent flow topology: (a) Streamlines from the emergent steady state of the twister flow in the presence of a nucleus. The nucleus is located on the anterior side close to the MT bed, and the separatrix of the flow is represented by the thin blue slice. The color code of the streamlines indicates the magnitude of the fluid velocity, and the arrow indicates the direction of circulation. We observe that the fluid flow slows down near the nucleus due to the no-slip boundary condition. The associated polarity field is shown below: (left) the same view angle as the twister flow reveals splaying of the MT polarity near the nucleus; (right) a rotated view shows the positioning of +1 topological defect. The anterior (A) and posterior (P) poles are labeled for convenience, and the defect locations are depicted by the black spheres. (b) The same is shown for a similar-sized geometric obstacle placed at the center of the egg cell. Unlike (a), the flow does not break AP symmetry and retains its robust almost axisymmetric structure. The streaming speed U_s for these calculations range between 200 and 300 nm/s.

Here $\llbracket a \rrbracket = a|_{\partial S^+} - a|_{\partial S^-}$ denotes the jump of any variable across the interface ∂S , and $\sigma = -q\mathbf{I} + (\nabla\mathbf{u} + \nabla\mathbf{u}^T)$ is the Newtonian stress tensor. The surface stress jump is given as

$$\bar{\mathbf{f}}(\mathbf{y}, t) = \bar{\rho}\bar{\sigma}\mathbf{P} + \bar{\rho}\chi \left[\mathbf{T}_0 \times \mathbf{P} - \frac{\mathbf{P}\mathbf{P}\mathbf{P}}{2} : \nabla\mathbf{u} \Big|_{\partial D} \right]. \quad (11)$$

The first term in Eq. (11) arises from the forces exerted by the kinesin-1 motor proteins on the fluid, and it is proportional to the density $\bar{\rho}$ and forcing from individual motor proteins $\bar{\sigma}$. The second term represents forces stemming both from the torsional spring and the rod's response in the mean-field fluid flow [25]; χ is a geometric parameter that depends on the aspect ratio of the MTs. Taken together, this model integrates a boundary force field as defined by Eq. (11) to an internal homogeneous Stokes flow delineated in Eqs. (8)–(10). The forcing and the emergent flow evolve self-consistently with a partial differential equation that details the polarity of the MT bed as laid out in Eq. (7). Further details about the model and simulations are provided in the Supplemental Material [7–10,16].

Figure 7 illustrates the steady-state flows computed using this coarse-grained model. While the global structure of the flow remained fairly robust, it now exhibits key differences from the cases without a nucleus. First, the flows are no longer axisymmetric due to the asymmetric positioning of the nucleus and the no-slip boundary condition on its surface. Second, we observed that the slowing down of the flows around the nucleus was accompanied by splaying of the surface polarity field in the MT orientation, as depicted in Fig. 7(a). Finally, the anterior-posterior symmetry breaking of the oocyte had interesting consequences for the weaker bitoroidal flow. In simulations with unperturbed prolate ellipsoids, the midplane of the oocyte served as a plane of symmetry that separated the recirculating regions arising from

the bitoroidal flow. In contrast, here the nucleus plays the role of a geometric separatrix of the toroidal flows on two asymmetric halves of the oocyte. These flows are topologically distinct and do not mix with one another (represented in Fig. 7 by the thin blue slice). We believe this could have significant implications in the context of transport and mixing of cytoplasmic contents. In conclusion, the results of the active carpet model provide further evidence that cytoplasmic streaming is robust to certain geometric perturbations. Though the local structure of the flow might be affected, the overall flow retains its axisymmetric and vortical structure.

III. DISCUSSION

There is relatively little understood about how the geometry of the cell affects the processes within it. We study this question in the important context of self-organized cytoplasmic streaming in the *Drosophila* oocyte. The idea that geometry can influence streaming is not unique to *Drosophila* oocytes. Evidence for large scale cytoplasmic movements goes back to work from Bonaventura Corti in 1774, which documents streaming in large *Nitella* algal cells [26]. Just as in the case of the *Drosophila* oocyte, many large algal cells have been found to use cytoplasmic movements to make up for the reduced efficiency of diffusion at relatively long length scales [27,28]. More recent work from Ref. [29] has explored a model in which the cylindrical geometry of *Chara* algae cells can organize the bidirectional flow of cytoplasm by setting a preferred direction for the actin filaments and motors which walk upon them.

In this work, we have used a combination of large scale simulations, live imaging experiments, and reduced models of cytoplasmic streaming. Our hydrodynamics simulations make a prediction about the role of geometry in the real system,

which we then confirmed experimentally. While observations of cytoplasmic streaming in *Drosophila* have been around since the 1980s, there has been no quantitative characterization of flows in late-stage oocytes [3,18,30]. In earlier-stage oocytes, previous studies relied on particle image velocimetry (PIV). We developed a single-particle tracking pipeline for tracking and visualizing inert particles in the flow, which allowed us to image deeper into the tissue. Additionally, the streaklines can be used to extract information about diffusive and advective components of finite-sized particles in the flow field. We extracted information about the average angle of the flow and handedness from max projections of the 3D time series. We were able to use the simulated 3D particle tracks to compare predictions from simulations and distinguish flow orientations, even from thin cortical slices. And we were able to confirm that the actual 3D flow field of the oocyte is in fact a vortical flow about the long axis of the ellipsoid using a newly developed light sheet protocol. Our experimental findings matched our computational predictions: self-organized vortical flow emerges and rotates consistently around the long axis of the cell with no bias in handedness.

How a system evolves from an initial configuration with many possible solutions to selecting a single solution is a challenging problem. However, prior to this work, it was unclear how geometry could contribute to the loss of solutions in this specific system. Numerically and experimentally, we argue that the domain of the container aids in reducing the number of possible flow orientations to just one: flow around the long axis. Results from the model are realized in the actual cell. Just as the simulations provide insight about the nature of the flow, the experimental results, too, provide insight about the accuracy of the simulations and underlying model. By showing, just as simulations predict, that there is a preferred direction of flow in real oocytes, we have strengthened both the evidence for the current biophysical model and our understanding of boundary-driven flows in oocytes. Our updated picture of cytoplasmic streaming paves the way for future work to characterize the functional properties of the flow, namely how it transports molecules and mixes yolk granules.

IV. MATERIALS AND METHODS

A. Fly stocks and genetics

Flies were raised on standard cornmeal fly food prepared by Princeton University, which was supplemented with active yeast 24–48 h before dissection. The stocks were kept at 25°C. The standard UAS system for targeted gene expression in *Drosophila* was used to visualize Staufen protein aggregates in the cytoplasmic flows. *UASp-scFv*; *UASp-Staufen-SunTag* flies [11] coexpressing scFv tagged GFP and SunTag tagged Staufen proteins were crossed to nos driver flies, *GAL4-nos.NGT* [31]. Staufen is recruited to the posterior in wild-type oocytes. However, in stage-12 oocytes, Staufen did not visibly bind to the posterior end of the imaging plane; thus fluorescent Staufen aggregates were used as an inert tracer particles.

B. Confocal live imaging

Female flies of the correct genotype were anesthetized on CO₂ pads and dissected in Schneider's Mix media sup-

plemented with insulin, fetal bovine serum (FBS), and streptomycin/penicillin, and pH adjusted as described by [32]. The egg chambers were imaged in MatTek 35 mm glass bottom culture dishes using a Nikon AX laser scanning confocal microscope and the NIS-Elements software at the CCB Scope Observatory at the Flatiron Institute. Imaging was performed using a 40×/1.2 silicon oil objective lens. Pinhole settings ranged from 1.0 to 1.2 Airy units. Excitation of the fluorophore, GFP, was performed at 489 nm. 3D volumes 15–20 μm deep were acquired every 10–20 s at 1 μm/step.

C. Image analysis and velocity field reconstruction

Fiji's TrackMate plugin was used to perform single-particle tracking on 2D max projection slices from 10 to 15 μm depth 3D volumes. The max projection was used to increase the resolution and was justified by the fact that the velocity field did not vary substantially in thin 10–15 μm cortical sections. The degree of Gaussian (DoG) filter was used to detect particles of diameter 1.5–2.5 μm, which corresponded to the average size of the imaged GFP-Staufen tracer particles. A linear assignment problem (LAP) tracker was used to connect particle trajectories and then filtered for trajectories of a minimum length. The average velocity fields were acquired by integrating information across the time lapse images. Because the flow fields were relatively stable in stage-12 oocytes, a steady-state flow was assumed. Each time point of a particle trajectory resulted in a local velocity vector at the instantaneous position of the particle. Velocity vectors from each time point in the movie were used to generate a velocity field. To interpolate the velocity field onto a structured grid, each vector within a 5 μm radius of a point on the structured grid was averaged. If there were fewer than 30 vectors within 5 μm, the radius of search was increased until there were 30 velocity vectors within the circle.

A least-squares method was used to fit an ellipse with semimajor axis, *A*, and semiminor axis, *B*, to the boundary of the oocyte. The long axis of the ellipse defined the anterior-posterior axis. To account for the fact that the edge of the oocyte is coated by a microtubule bed, only data within 3/4th of the semimajor and semiminor axes were considered. The interpolated velocity field was binned along the length of the long axis and the mean vector was calculated. The angle, θ , was reported with respect to the long axis of the cell. The handedness of the flow was counted with respect to the posterior of the cell.

We were careful in correlating velocity profiles from image slices near the cortex to entire flow fields in the oocyte because we were dealing with an ill-posed inverse problem. Nearly identical slices near the cortex with similar θ 's could correspond to different flow fields in the body. Our experimental result is consistent with sampling from axisymmetric or close to axisymmetric flow orientations. Therefore, the distribution of θ 's from Fig. 3 in which θ is peaked around 90° indicates a predominance of near “axisymmetric” flows, just as predicted by simulation (Fig. 2).

3D particle tracks were extracted using the DoG filter and nearest-neighbor algorithm in Fiji's TrackMate plugin. Ellipses were fit using least squares to every slice in the z-stack, and the resulting stack of ellipses and their known z-spacing

was used to fit the entire oocyte to an ellipsoid. The long axis of the ellipsoid was set as the x -axis, and the direction of the z -stack was set as the z -axis. Within this coordinate system, the 3D streaklines were used to obtain information about the relative magnitude particle velocity components, v_x , v_y , and v_z .

D. Multiview light sheet imaging and reconstruction

A FEP tube, which is index matched to the media, was attached to the standard glass capillary used in Bruker's Multi-View Selective-Plane Illumination Microscope (MuVi SPIM) and the capillary/FEP tube apparatus was filled with 5% agar solution such that \sim 1 mm of the FEP tube was filled. The solution, which was embedded with 0.1 μm fluorescent Tetraspeck microspheres, was allowed to harden and fresh Schneider's Mix was pipetted into the FEP tube. A single oocyte was carefully dropped into the FEP tube such that it rested on the bed formed by the agar surface, while surrounded by the media. The FEP tube was capped with mineral oil to prevent evaporation. This enabled the oocyte to develop normally for at least an hour. The oocyte was imaged from two perpendicular directions at a z -spacing smaller than the PSF of the scope. An image analysis pipeline from [23] was used to register the two angles and deconvolve the images using the PSF of the microspheres. The result was an isotropic 3D video with 1347 z -planes.

Due to the low signal-to-noise ratio of light sheet imaging, it was not possible to visualize particles deep into the oocyte.

Additionally, the videos were plagued with shadows from yolk granules, and the particles could not be tracked using common image processing techniques. Instead, each visible particle was manually tracked in the following manner. A max projection of 100 slices was performed every 50 slices. The z -value of the pixel with the highest intensity was stored at each timepoint. The manual tracking was performed for each of the 36 maximum intensity projections, and the information about the z -position of each pixel was used to back out the 3D streaklines.

ACKNOWLEDGMENTS

We wish to especially acknowledge the help and guidance of David Stein. Additionally, we wish to thank Wen Lu, Vladimir Gelfand, Manas Rachh, Jasmin Imran Alsous, Howard Stone, and Surya Maddu for valuable discussions. We wish to thank Wen Lu and Vladimir Gelfand for their generous contribution of the fly lines used in all experiments. B.C. acknowledges the support of the Department of Atomic Energy, Government of India, under Project No. RTI4001. We acknowledge support from the CCB_X program of the Center for Computational Biology of the Flatiron Institute. The experimental observations reported in this work were performed in the CCBScope Observatory at the Flatiron Institute. This material is based upon work supported by the National Science Foundation Graduate Research Fellowship under Grant No. DGE-2039656 (A.O.J.).

-
- [1] S. Bialecki, B. Kazmierczak, and T. Lipniacki, Polarization of concave domains by traveling wave pinning, *PLoS ONE* **12**, e0190372 (2017).
 - [2] P. Pintado, P. Sampaio, B. Tavares, T. D. Montenegro-Johnson, D. J. Smith, and S. S. Lopes, Dynamics of cilia length in left-right development, *R. Soc. Open Sci.* **4**, 161102 (2017).
 - [3] M. E. Quinlan, Cytoplasmic streaming in the *Drosophila* oocyte, *Annu. Rev. Cell Dev. Biol.* **32**, 173 (2016).
 - [4] S. Dutta *et al.*, Self-organized intracellular twisters, *Nat. Phys.* **20**, 666 (2024).
 - [5] K. M. Forrest and E. R. Gavis, Live imaging of endogenous RNA reveals a diffusion and entrapment mechanism for nanos mRNA localization in *Drosophila*, *Curr. Biol.* **13**, 1159 (2003).
 - [6] D. B. Stein and M. J. Shelley, Coarse graining the dynamics of immersed and driven fiber assemblies, *Phys. Rev. Fluids* **4**, 073302 (2019).
 - [7] D. B. Stein, G. D. Canio, E. Lauga, M. J. Shelley, and R. E. Goldstein, Swirling instability of the microtubule cytoskeleton, *Phys. Rev. Lett.* **126**, 028103 (2021).
 - [8] R. M. Parton, R. S. Hamilton, G. Ball, L. Yang, C. F. Cullen, W. Lu, H. Ohkura, and I. Davis, A par-1-dependent orientation gradient of dynamic microtubules directs posterior cargo transport in the *Drosophila* oocyte, *J. Cell Biol.* **194**, 121 (2011).
 - [9] C. E. Monteith, M. E. Brunner, I. Djagaeva, A. M. Bielecki, J. M. Deutsch, and W. M. Saxton, A mechanism for cytoplasmic streaming: Kinesin-driven alignment of microtubules and fast fluid flows, *Biophys. J.* **110**, 2053 (2016).
 - [10] W. Lu, M. Winding, M. Lakonishok, J. Wildonger, and V. I. Gelfand, Microtubule-microtubule sliding by kinesin-1 is essential for normal cytoplasmic streaming in *Drosophila* oocytes, *Proc. Natl. Acad. Sci. USA* **113**, E4995 (2016).
 - [11] W. Lu, M. Lakonishok, A. S. Serpinskaya, D. Kirchenbuechler, S. C. Ling, and V. I. Gelfand, Ooplasmic flow cooperates with transport and anchorage in *Drosophila* oocyte posterior determination, *J. Cell Biol.* **217**, 3497 (2018).
 - [12] Ö. Civalek and Ç. Demir, Bending analysis of microtubules using nonlocal Euler-Bernoulli beam theory, *Appl. Math. Modell.* **35**, 2053 (2011).
 - [13] E. Orlandini, D. Marenduzzo, and A. B. Goryachev, Domain formation on curved membranes: Phase separation or turing patterns? *Soft Matter* **9**, 9311 (2013).
 - [14] N. Okabe, B. Xu, and R. D. Burdine, Fluid dynamics in zebrafish Kupffer's vesicle, *Dev. Dyn.* **237**, 3602 (2008).
 - [15] F. Institute, *Skellysim* (2023).
 - [16] See Supplemental Material at <http://link.aps.org/supplemental/10.1103/PRXLIFE.3.023007> for additional details about the flow simulations.
 - [17] M. J. Shelley, Flows, self-organization, and transport in living cells, *Phys. Rev. Fluids* **9**, 120501 (2024).
 - [18] H. O. Gutzeit and R. Koppa, Time-lapse film analysis of cytoplasmic streaming during late oogenesis of *Drosophila*, *J. Embryol. Exp. Morphol.* **67**, 101 (1982).
 - [19] W. E. Theurkauf, S. Smiley, M. L. Wong, and B. M. Alberts, Reorganization of the cytoskeleton during *Drosophila* oo-

- genesis: Implications for axis specification and intercellular transport, *Development* **115**, 923 (1992).
- [20] W. E. Theurkauf, B. M. Alberts, Y. N. Jan, and T. A. Jongens, A central role for microtubules in the differentiation of *Drosophila* oocytes, *Development* **118**, 1169 (1993).
- [21] J. Januschke, L. Gervais, L. Gillet, G. Keryer, M. Bornens, and A. Guichet, The centrosome-nucleus complex and microtubule organization in the *Drosophila* oocyte, *Development* **133**, 129 (2006).
- [22] J. I. Alsous, N. Romeo, J. A. Jackson, F. M. Mason, J. Dunkel, and A. C. Martin, Dynamics of hydraulic and contractile wave-mediated fluid transport during *Drosophila* oogenesis, *Proc. Natl. Acad. Sci. USA* **118**, e2019749118 (2021).
- [23] T. Stern, S. Y. Shvartsman, and E. F. Wieschaus, Deconstructing gastrulation at single-cell resolution, *Curr. Biol.* **32**, 1861 (2022).
- [24] J. A. Lepesant, F. Roland-Gosselin, C. Guillemet, F. Bernard, and A. Guichet, The importance of the position of the nucleus in *Drosophila* oocyte development, *Cells* **13**, 201 (2024).
- [25] B. Chakrabarti, M. Rachh, S. Y. Shvartsman, and M. J. Shelley, Cytoplasmic stirring by active carpets, *Proc. Natl. Acad. Sci. USA* **121**, e2405114121 (2024).
- [26] B. Corti, *Osservazione Microscopiche sulla Tremella e sulla Circulazione del Fluido in Una Planto Acquaguola* (Appresso Giuseppe Rocchi, Lucca, Italy, 1774).
- [27] R. E. Goldstein and J.-W. van de Meent, A physical perspective on cytoplasmic streaming, *Interface Focus* **5**, 20150030 (2015).
- [28] W. F. Pickard, Hydrodynamic aspects of protoplasmic streaming in *Chara Braunii*, *Protoplasma* **82**, 321 (1974).
- [29] F. G. Woodhouse and R. E. Goldstein, Cytoplasmic streaming in plant cells emerges naturally by microfilament self-organization, *Proc. Natl. Acad. Sci. USA* **110**, 14132 (2013).
- [30] H. O. Gutzzeit, The role of microfilaments in cytoplasmic streaming in *Drosophila* follicles, *J. Cell Sci.* **80**, 159 (1986).
- [31] W. D. Tracey Jr., X. Ning, M. Klingler, S. G. Kramer, and J. P. Gergen, Quantitative analysis of gene function in the *Drosophila* embryo, *Genetics* **154**, 273 (2000).
- [32] M. Prasad, A. C. Jang, M. Starz-Gaiano, M. Melani, and D. J. Montell, A protocol for culturing *Drosophila melanogaster* stage 9 egg chambers for live imaging, *Nat. Protoc.* **2**, 2467 (2007).